Enhancing underwater optical imaging by using a low-pass polarization filter

Khadidja Ould Amer, Marwa El Bouz, Christian Brosseau, Jaouad Hajjami, Ayman Alfalou

Research Article | Vol. 27, No. 2 | 21 Jan 2019 | OPTICS EXPRESS 621
Optics EXPRESS

Enhancing underwater optical imaging by using a low-pass polarization filter

KHADIDJA OULD AMER,[1] MARWA ELBOUZ,[1] AYMAN ALFALOU,[1,*] CHRISTIAN BROSSEAU,[2] AND JAOUAD HAJJAMI[1,3]

[1]*Vision Lab. ISEN Brest, L@bISEN, 20 rue Cuirassé Bretagne, CS 42807 29228 Brest Cedex 2, France*
[2]*Univ. Brest, Lab-STICC, CNRS, 6 avenue Le Gorgeu, CS 93837 29238 Brest Cedex 3, France*
[3]*Forssea Robotics, 130 rue de Lourmel 75015 Paris, France*
**ayman.al-falou@isen-bretagne.fr*

Abstract: Object identification in highly turbid optical media depends mainly on the quality of collected images. Underwater images acquired in a turbid environment are generally of very poor quality. Attenuation and backscattering of light by water, by materials dissolved in the water, and by particulate material are the main causes of the degradation of underwater images. It is therefore essential to improve the quality of such images to facilitate object identification. The focus of this paper is to report the principle and validation of a fast and effective method of improving the quality of underwater images. On the one hand, this method uses a polarimetric imaging optical system to reduce the effect of diffusion on the image acquisition. On the other hand, it is based on an optimized version of the dark channel prior (DCP) method that has received a great deal of attention for image dehazing. Results derived from images obtained in a controlled laboratory water tank environment with different turbidity conditions and images from tests using the proposed method at sea demonstrate an ability to significantly improve visibility and reduce runtime by a factor of about 50 for a 4K image when compared to conventional DCP methods.

1. Introduction

1.1 Background

Most underwater (scientific, industrial or military) vehicles are equipped with at least one embedded camera to observe and analyze the seabed. Typically, these remote operated vehicles (ROV) are often operated by crew operators aboard a research vessel. The ROV has an umbilical cable that contains electrical cables and optical fibers to carry electrical power, data and video signals [1]. Tethering systems to ROVs impose speed and depth restrictions that limit maneuverability. In addition, human intervention implies that the treatment is often long, tedious and dangerous. Such issues can be reduced by the use of autonomous underwater vehicles (AUV). The AUV is an untethered underwater robot that carries out a mission fully autonomously even without communication with crew operators. However, the treatment and the automatic analysis of acquired images are limited by the very bad quality of underwater images which decreases the performance of the detection and object recognition algorithms. Absorption and scattering of light by water, by materials dissolved in the water, and by particulate material are the main causes of the degradation of these images. Morel [2], give excellent reviews of the associated physics and mathematics. Both phenomena are highly wavelength dependent and depend also on the size of the particles within the water which also governs the type of scattering that occurs, namely Mie or Rayleigh scattering [3]. Blue light penetrates deeper than red light (Fig. 1).

#347432 https://doi.org/10.1364/OE.27.000621
Journal © 2019 Received 3 Oct 2018; revised 14 Nov 2018; accepted 14 Nov 2018; published 8 Jan 2019

Optics EXPRESS

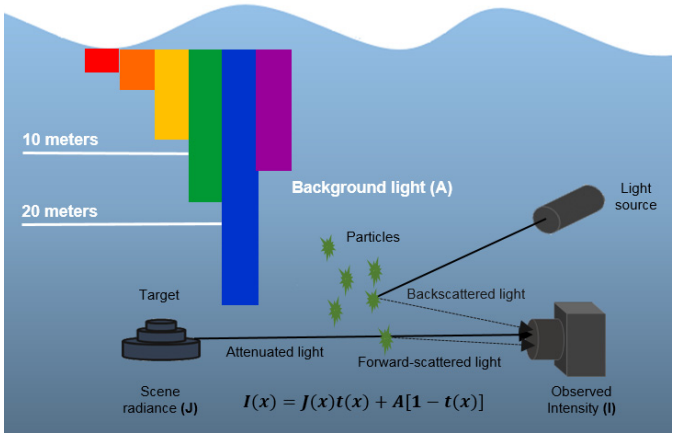

Fig. 1. Absorption and scattering in water.

One of the major difficulties inherent in the treatment of the collected underwater images comes from the exponential attenuation of light which limits visibility to around 20 *m* in clear water and to less than 5*m* in turbid water [4]. A useful background underwater image model of formation has been proposed by Jaffe [5]. This assumes that the underwater image I received by the camera is the sum of three components, i.e. direct attenuation I_A, forward scattering I_F and backscattering I_B such as:

$$I(x) = I_A(x) + I_F(x) + I_A(x) \tag{1}$$

where x denotes image coordinates. According to Schechner and Karpel [6], backscattering is the main reason for deterioration of the underwater visibility, thus forward scattering can be neglected.

This assumption is valid when the distance between the scene and the camera is large. Equation (1) can be written as:

$$I(x) = I_A(x) + I_B(x) \tag{2}$$

or

$$I(x) = J(x)t(x) + A(1 - t(x)) \tag{3}$$

In Eq. (3), $I(x)$ is the intensity observed at pixel x composed of the scene radiance $J(x)$ mixed with light arising from the background light A according to the optical medium transmission coefficient [7]. The transmission map describes the portion of the scene $J(x)t(x)$ which has not been scattered or absorbed through the optical medium and which reached the camera. When the optical medium is assumed to be homogeneous, the transmission map $t(x)$ is often estimated as an exponential form:

$$t(x) = \exp(-\beta \cdot d(x)) \tag{4}$$

where β is the scattering coefficient of the optical medium (β is close to 0 in clear water conditions) and d is the scene depth. The backscattered light, $(1 - t(x))$, comes from the interaction between the propagating light and particles dispersed in the optical medium according to the transmission map. As we can see, if ($t(x) \to 0, I(x) = A$). Furthermore,

Optics EXPRESS

forward scattering causes a blur in the image while backscattering produces a light veil which reduces the contrast and visibility of the observed scene [4]. Additionally, using artificial lighting to improve visibility introduces shadows and illuminates the scene in a non-uniform way. Both phenomena make it difficult, even impossible, to detect and/or identify objects in strongly turbid optical media.

1.2 State-of-the-art

Many techniques of restoration and improvement of the quality of the underwater images have been proposed in the archival literature and this continues to be a timely subject of research [8]. Restoration techniques are designed to assess the degradation of the image during its acquisition and then to apply an inverse transform of the model to recover the original image. Deconvolution of the water transfer function is in principle possible for restoration of underwater images [9]. Hou and associates [10] incorporated optical properties of water in the transfer function of an underwater camera system. Trucco and Olmos-Antillon [11] presented a self-adjusting restoration filter based on a simplified model of underwater image formation. Ouyang and associates [12] used pulsed laser light and a bilateral filtering method based on deconvolution for underwater image enhancement. Schechner and Treibitz [13] suggested an effective algorithm that requires two polarized images obtained in two orthogonal directions to restore the original scene. Although these approaches were being introduced for improving the physical contrast of simple images, they require many unknown parameters (such as the attenuation coefficients of the medium and depth of the scene) which can be difficult of estimating with precision. In addition, these methods use relatively expensive and complex optical components such as e.g. a range-gated laser. Furthermore, solutions that require many image entries are usually difficult to apply because the acquisition of multiple images of the same scene is difficult in underwater conditions. In recent years, He and associates [7] suggested the DCP that allows estimating the depth of a scene from a single image and restoring the image without fog. Several studies used DCP to remove the luminous veil and adapted it to underwater conditions [14,15]. In contrast to restoration analysis, methods to improve quality do not rely on physical models and do not require an a priori knowledge of the environment. These methods use qualitative subjective criteria to improve the visual quality of the image, to reduce the noise and to correct color. To overcome the issue of non-uniform illumination in underwater images, Garcia and associates [16] proposed applying a homomorphic filtering. Hitam and associates [17] applied adaptive histogram equalization for underwater image enhancement. Ghani and Isa [18] suggested dividing the histogram of the image in the middle and stretching the two histograms obtained over the entire dynamic range following the Rayleigh distribution. Ancuti and associates [19] adopted another strategy by merging images derived from the original degraded image. Bazeille and associates [20] suggested an automatic algorithm consisting of several independent steps of treatment allowing correcting non-uniform lighting, eliminating noise, improving contrast and equalizing colors. Despite the simplicity and the multitude of digital methods designed for improving quality, their efficiency decreases as turbidity is increased. The combination of several numerical methods increases the runtime which is not desirable for any real-time application. For this specific reason, two approaches will be combined in this study. On the one hand, our method uses a polarimetric imaging optical system to reduce the effect of diffusion on the image acquisition. On the other hand, the method is based on an optimized version of the dark channel prior (DCP) method that has received a great deal of attention for image dehazing.

1.3 Motivation and outline

A question that often appears throughout the literature asks is that of the extent to which quality of underwater images can be improved while reducing algorithm runtime in order to facilitate real-time object identification?. This challenge is of importance when targeting

Optics EXPRESS

underwater objects. In this paper, computational and experimental investigations show the effect of turbidity on visibility and algorithm runtime of collected images. The successful performance of the method developed in the paper is illustrated by considering images obtained in underwater field experiments either in a controlled laboratory water tank environment with different turbidity conditions and or from tests at sea.

2. Imaging polarimetry

In this section, we offer a brief background as well as a set of definition of terms that are used in the paper. Then, preliminary tests document the benefit of incorporating polarization information into the algorithm.

2.1 State of the art

Polarimetry has been widely as a useful technique that removes degradation effects in underwater vision [6,21–24]. The propagation of polarized light in water has led to the development of active and passive polarimetric imaging systems. Passive imaging uses the ambient light from the sun that is unpolarized. The light that does not reach the object becomes partially polarized by scattering and can be filtered by an analyzer placed in front of the detector [6]. However, natural light illumination is inapplicable at great depth where active scene irradiance is required. Active imaging requires artificial light illumination and appropriate detection scheme. Several studies have proposed to exploit the differences in polarimetric responses between target and backscattering [25,26]. A comprehensive study of polarimetric backscatterd light variations was considered in [25]. The backscattered Mueller matrix for various concentrations of spherical scatterers with and without painted metal target was measured. However, such measurements are time consuming because they often require considerable data acquisition. More recent studies proved that the strong backscatter created by artificial lighting can be reduced by performing a single acquisition with adapted input and output polarization states. The evolution of circularly and linearly polarized states of light as they scatters throughout an optical medium composed of particles in suspension in water (e.g. randomly scattering media of a polystyrene-microsphere solution), numerical simulation, analytical theory and experimental data have shown that circularly polarized light exhibits superior persistence (compared to linearly polarized light) for forward-scattering particulate medium [27–34]. Assuming that the target is totally depolarizing and handedness of the circularly polarized state change after reflection by the scattering particles, Gilbert and associates [27] showed that using circularly polarized light permits reduction of backscatter and increase by a factor of two of the visibility range compared to intensity measurements. Mullen and associates [34] provided a technique using polarization discrimination for analyzing the contribution of backscattered light, arising from multiple scattering of the interrogating laser beam from water particulate matter in both the forward and backward directions, and improving the contrast of the retro-reflected signal. These authors evidence that both the light forward scattered on its path to and from an underwater object and the light that is scattered back to the detector without reaching the object have a high degree of polarization when linearly polarized light is transmitted.

2.2 Characterization of underwater object

The detection of an underwater target by use of polarization discrimination depends on the different polarimetric responses between the target and scattering medium which separates the object from the camera. Several studies have focused on characterizing the transport of polarized light through different scattering media by means of the Stokes-Mueller formalism [25]. This enables to completely describe the effect of the scattering medium or the target on an incident polarized light via Mueller matrices. A Stokes vector S is a four-component vector defined as:

Optics EXPRESS

$$S = \begin{pmatrix} I \\ Q \\ U \\ V \end{pmatrix} \tag{5}$$

Where I represents the total intensity of the detected light, and Q,U,V defined by

$$\begin{aligned} I &= E_{0x}^2 + E_{0y}^2 \\ Q &= E_{0x}^2 - E_{0y}^2 \\ U &= 2E_{0x}E_{0y}\cos\phi \\ V &= 2E_{0x}E_{0y}\sin\phi \end{aligned} \tag{6}$$

where E_{0x} and E_{0y} denote the amplitudes of the parallel and perpendicular to the scattering plane electric field components and ϕ is the relative phase difference. The polarization state of the scattered light S' can be written as:

$$S' = M \cdot S \Leftrightarrow \begin{pmatrix} I' \\ Q' \\ U' \\ V' \end{pmatrix} = \begin{pmatrix} m_{11} & m_{12} & m_{13} & m_{14} \\ m_{21} & m_{22} & m_{23} & m_{24} \\ m_{31} & m_{32} & m_{33} & m_{34} \\ m_{41} & m_{42} & m_{43} & m_{44} \end{pmatrix} \cdot \begin{pmatrix} I \\ Q \\ U \\ V \end{pmatrix} \tag{7}$$

where the 16 M_{ij} elements define the Mueller matrix. In pure water containing Rayleigh spherical scatters, single scattering events dominate over multiple scattering and absorption can be neglected. Within these assumptions, the normalized Mueller matrix is [26,33]

$$M = \begin{pmatrix} 1 & M_{12}(\theta) & 0 & 0 \\ M_{12}(\theta) & 1 & 0 & 0 \\ 0 & 0 & M_{33}(\theta) & 0 \\ 0 & 0 & 0 & M_{33}(\theta) \end{pmatrix} \tag{8}$$

where θ is the scattering angle and

$$\begin{aligned} M_{11} &= M_{22} = 1 \\ M_{12}(\theta) &= M_{21}(\theta) = \frac{-1+\cos^2(\theta)}{1+\cos^2(\theta)} \\ M_{33}(\theta) &= M_{44}(\theta) = \frac{2\cdot\cos(\theta)}{1+\cos^2(\theta)} \end{aligned} \tag{9}$$

For backscattering conditions ($\theta = 180^\circ$), Eq. (8) becomes

$$M = \begin{pmatrix} 1 & 0 & 0 & 0 \\ 0 & 1 & 0 & 0 \\ 0 & 0 & -1 & 0 \\ 0 & 0 & 0 & -1 \end{pmatrix} \tag{10}$$

Optics EXPRESS

Backscattering from Rayleigh spheres preserves the linear polarization state of the incident light (vertical or horizontal), while the handedness of the circularly polarized light is reversed after a backscattering event. For turbid water conditions, experiments have shown that the scattering regime can be described with a matrix which is very similar to Eq. (10) but containing the supplemental elements M_{34} and M_{43} satisfying $M_{43} = -M_{34}$ [26]. Nevertheless, for backscatter-ring condition, ($\theta = 180^{\circ}$) linear polarization is preserved and circular helicity is reversed. This backscattering conservation property is widely used for underwater target detection by controlling the polarization state of the light source and the camera through suitable combination of polarizers. Indeed, imaging with cross-polarization state using linearly polarized light and co-polarized state using circularly polarized light better discriminates the useful signal from backscattering. However, in practice this method can be effective only if the target is sufficiently depolarizing. Other studies have demonstrated that performing measurements with two orthogonal states permits decreasing the backscattering effect. Treibitz and Schechner [6] presented an approach for recovering the object signal using polychromatic polarized light illumination. The camera is fitted with a polarization analyzer. Two frames of the scene are taken, with different states of the analyzer or polarizer. A recovery algorithm follows the acquisition. This method allows both the backscatter and the object reflection to be partially polarized. The algorithm assumes that the underwater image is made up of the target signal and the backscattered signal. We will write the measured image in the following typical form:

$$I(x,y) = S(x,y) + B(x,y) \tag{11}$$

where $S(x,y)$ is the signal from target and $B(x,y)$ corresponds to the backscatter. Two images $I_{\min}$ and $I_{\max}$ are acquired, corresponding respectively to the linear cross-polarization image (co-circular) and the linear-parallel image (cross-circular). The linear cross-polarization (co-circular) image $I_{\min}$ is obtained when the analyzer is placed in the orthogonal (resp. same) state of the light source polarizer. The linear parallel polarization (cross-circular) image $I_{\max}$ is obtained when the analyzer is placed in the same (resp. orthogonal) state of the light source polarizer. As a large fraction of the linear (circular) polarization is preserved (reversed) under wide-angle backscattering, this technique in the cross-state (co-circular) yields an image with less backscatter and target signal. Thus, the images are expressed as:

$$I_{\max}(x,y) = S_{\max}(x,y) + B_{\max}(x,y) \tag{12}$$

$$I_{\min}(x,y) = S_{\min}(x,y) + B_{\min}(x,y) \tag{13}$$

The degree of polarization (DOP) of the target and backscatter are written, respectively, as:

$$P_{t\arg} = \frac{S_{\max}(x,y) - S_{\min}(x,y)}{S_{\max}(x,y) + S_{\min}(x,y)} \tag{14}$$

and

$$P_{scat} = \frac{B_{\max}(x,y) - B_{\min}(x,y)}{B_{\max}(x,y) + B_{\min}(x,y)} \tag{15}$$

The target and the backscatter signals can be expressed as:

$$S(x,y) = S_{\max}(x,y) + S_{\min}(x,y) \tag{16}$$

and

Optics EXPRESS

$$B(x,y) = B_{\max}(x,y) + B_{\min}(x,y) \tag{17}$$

Equations (18) and (19) can be used to provide an estimate of the target $\tilde{S}$ and backscattering $\tilde{B}$ as respectively:

$$\tilde{S} = \frac{1}{P_{scat} - P_{t\arg}}\left[I_{\min}(1+P_{scat}) - I_{\max}(1-P_{scat})\right] \tag{18}$$

$$\tilde{B} = \frac{1}{P_{scat} - P_{t\arg}}\left[I_{\min}(1-P_{scat}) - I_{\min}(1+P_{scat})\right] \tag{19}$$

The target estimate can thus be inferred from measures of $I_{\min}$ and $I_{\max}$, for a given value of P_{scat}, since $P_{t\arg}$ does contribute only to a scale factor for the reconstruction of the signal. The target estimate can be done on the basis of Eq. (18) assuming that $P_{targ} = 0$. It should be noted that the value of P_{scat} is crucial and must be assessed with precision. We note that this method has been used in [22], and it gives good results. However, it is difficult to use it for the current application at least for two reasons. Firstly, the acquisition of two images of the same scene is difficult without human intervention because of the rapid changes of the 3D scene structure and light illumination conditions. Second, the estimate of P_{scat} requires a precise selection of an image area where the target does not appear, which is difficult to implement automatically. This is the reason why this study considers a single polarization measure that minimizes the backscattering effect in the image.

2.3 Experimental setup

Since the nature of the object to be identified is unknown, it remains difficult to estimate its depolarization properties. Consequently, no optimized state of polarization can be guessed. In this work, we try to use polarization states allowing us to get images with the best quality. Two polarization options are considered, either a linearly co-polarized or a cross-polarized scheme. The experimental set-up used is depicted in Fig. 2.

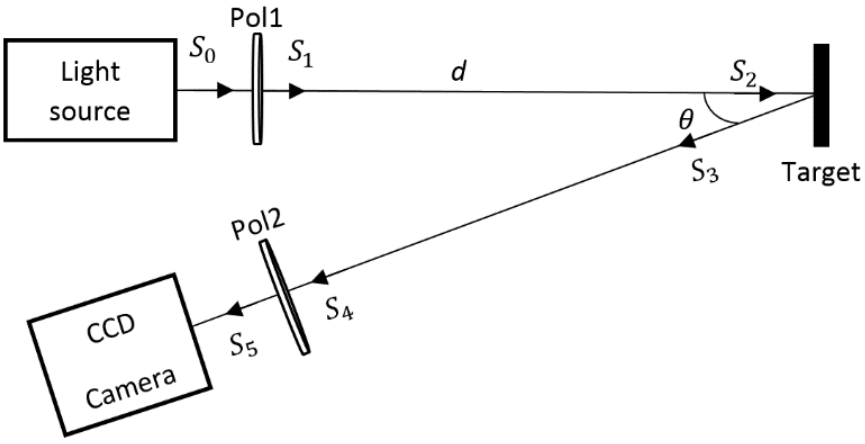

Fig. 2. Experimental setup for underwater target detection. Pol1 is a linear polarizer, Pol2 is a linear analyzer, and S_i denotes Stokes vector i.

The image obtained for the linear parallel polarization state $I_{\parallel}$ (resp. ($I_{\perp}$)) is obtained when the analyzer Pol2 is placed in the same (resp. orthogonal) state of polarizer Pol1 of the

Optics EXPRESS

light source. During the light transport from the source to the CCD camera, light polarization changes and can be mathematically described by a matrix product with: the Mueller matrix of the polarizer Pol1 ($S_1 = M_{pol1}S_0$), Mueller matrix of water (source-target M_{w1} ($S_2 = M_{w1}S_1$)/target-camera M_{w2} ($S_4 = M_{w2}S_3$)),Mueller matrix of the target $M_{t\arg}$ ($S_3 = M_{t\arg}S_2$) and Mueller matrix M_{Pol2} of the analyzer Pol2 ($S_5 = M_{pol2}S_4$). Thus, the Stokes vector S_5 that characterizes the polarization state of light received by the CCD camera can be written as:

$$S_5 = M_{pol2}M_{w2}M_{t\arg}M_{w1}M_{pol1}S_0 \tag{20}$$

We make three more assumptions:(i) the light source is completely unpolarized and characterized by the Stokes vector $S_0 = \begin{pmatrix} S_{00} & 0 & 0 & 0 \end{pmatrix}^T$, where S_{00} is the total intensity of the wave, (ii) the Mueller matrix of the underwater target $M_{t\arg}$ is

$$M_{t\arg} = \begin{pmatrix} m_{11} & m_{12} & m_{13} & m_{14} \\ m_{21} & m_{22} & m_{23} & m_{24} \\ m_{31} & m_{32} & m_{33} & m_{34} \\ m_{41} & m_{42} & m_{43} & m_{44} \end{pmatrix} \tag{21}$$

And (iii) the Mueller matrix of water (source-target M_{w1} / target-camera M_{w2}) are also unknown because we cannot specify the effect of turbidity of the seabed during image acquisition. However, based on the fact that backscattering conserves linear polarization and reverse circular helicity, we assume that:

$$M_{w1} = M_{w2} = \begin{pmatrix} 1 & 0 & 0 & 0 \\ 0 & 1 & 0 & 0 \\ 0 & 0 & -1 & 0 \\ 0 & 0 & 0 & -1 \end{pmatrix} \tag{22}$$

Knowing that the Mueller matrix of a linear polarizer is:

$$M_{pol} = \frac{1}{2}\begin{pmatrix} 1 & \cos(2\varphi) & \sin(2\varphi) & 0 \\ \cos(2\varphi) & \cos^2(2\varphi) & \cos(2\varphi)\sin(2\varphi) & 0 \\ \sin(2\varphi) & \cos(2\varphi)\sin(2\varphi) & \sin^2(2\varphi) & 0 \\ 0 & 0 & 0 & 0 \end{pmatrix} \tag{23}$$

Where φ is the polarization angle, the parallel polarization image $I_{\backslash\backslash}$ is obtained when the same polarization angle for Pol1 and Pol2 ($\varphi_{pol1} = \varphi_{pol2} = 90^\circ$) is fixed and we get

$$I_{\backslash\backslash} = \frac{1}{4}\begin{pmatrix} m_{t11} + m_{t12} + m_{t21} + m_{t22} \\ m_{t11} + m_{t12} + m_{t21} + m_{t22} \\ 0 \\ 0 \end{pmatrix} \cdot S_{00} \tag{24}$$

Similarly, the orthogonal polarization image $I_{\perp}$ is obtained when the polarization angles for Pol1 and Pol2 are fixed to orthogonal states ($\varphi_{pol1} = 90^\circ, \varphi_{pol2} = 0^\circ$) and we get:

Optics EXPRESS

$$I_{\perp} = \frac{1}{4}\begin{pmatrix} m_{t11} + m_{t12} - m_{t21} - m_{t22} \\ m_{t21} - m_{t12} + m_{t11} + m_{t22} \\ 0 \\ 0 \end{pmatrix} \cdot S_{00} \tag{25}$$

2.4. Tests in small water tank

In this part we present our first tests that were carried out in a controlled laboratory water tank (15 *L* of natural water) environment with different turbidity conditions by adding milk [35]. Milk is a complex biological fluid composed of water, fat, protein, lactose, organic acids, and inorganic compounds. These different kinds of particles in milk change its scattering properties based on their differences in size, concentration and optical properties. Skim milk contains casein micelles with size polydispersity in the range between 0.04 and 0.3 *mm* (Rayleigh scattering regime). Skim milk appears slightly blue because the small casein micelles predominantly scatter the shorter wavelengths of visible light. In addition, low-fat milk contains fat droplets with size in the range 1-20 *mm*, corresponding to Mie scattering regime. Thus, for a concentration *c* (in %) of milk in a certain volume of water, an estimate for the diffusion coefficient is respectively $\mu_s = 1.40c \cdot cm^{-1}$ for low-fat milk and $\mu_s = 0.42c \cdot cm^{-1}$ for skim milk [36]. For the wavelength considered in our tests, the absorption properties in light scattering can be ignored. The optical thickness τ_0 is defined as the product of the coefficient of reduction μ_s and the distance *d* between the object and the camera, such as $\tau_0 = \mu_s \cdot d$ .If $\tau_0 >> 1$ light is multiply scattered while light is singly scattered if $\tau_0 << 1$. Figure 3, shows the experimental set-up used to acquire tests images. As can be seen in Fig. 3(b), the target (capital letter "A") is placed at the bottom of the water tank at a distance of 34 *cm* of a digital camera Sealife DC1400 video pro Set digital camera [37]: high resolution 14 megapixel CCD sensor, 26 *mm* lens wide angle, 20 MB memory internal, underwater vision field of 51° and can operate up to 60 *m* depth.

(a) *(b)*

Fig. 3. (a) Light source and camera with polarizers. (b) The used experimental set-up based on polarization.

The target is illuminated by a light source made by three white LEDs on which a linear polarizer is set. A linear analyzer is placed in front of the camera Fig. 3(a). The image obtained for the linear parallel polarization state ($I_{\parallel}$) (resp. ($I_{\perp}$)) is obtained when the analyzer is placed in the same (resp. orthogonal) state of polarization as the light source.

Optics EXPRESS

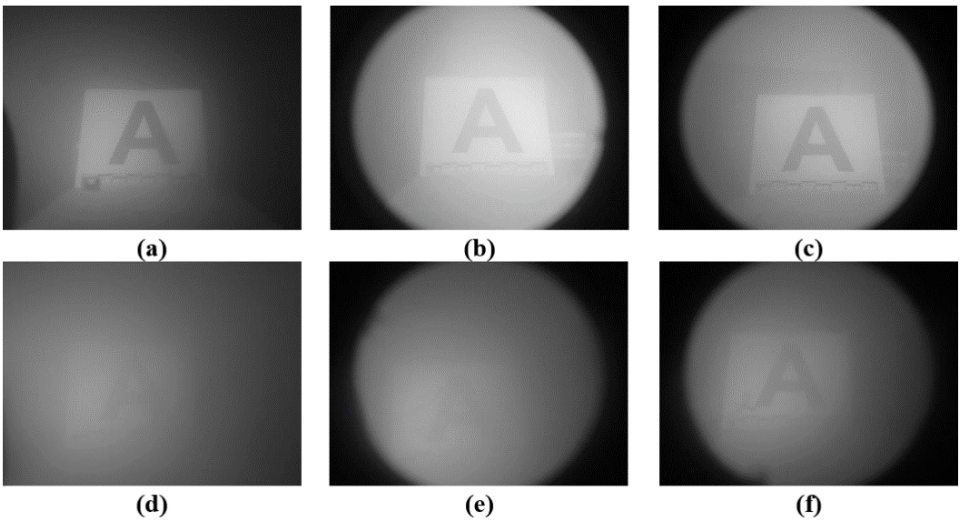

Fig. 4. Images of the target for two different turbidity conditions (top row: $\mu_s = 0.056cm^{-1}, \tau_0 = 1.96$), (bottom row $\mu_s = 0.084cm^{-1}, \tau_0 = 2.94$). (a) and (d): unpolarized images; (b) and (e) parallel polarization images; (c) and (f). Cross-perpendicular polarization images.

Figures 4(a) and 4(d) show the images acquired for two different turbidity conditions: Fig. 4(a) is obtained when 2 *cl* of skim milk is dispersed in 15*L* of water, the estimated diffusion coefficient is $\mu_s = 0.056cm^{-1}$. The distance traversed by light to attain the camera is d = 35cm corresponding to $\tau_0 = 1.96$. Similarly, Fig. 4(d) is characterized by $\mu_s = 0.084cm^{-1}$ and $\tau_0 = 2.94$. We can see from these images that the target is not visible in images taken without the use of the analyzer (Fig. 4(a) and Fig. 4(d)) and also in the image in the linear parallel analyzed polarization (Fig. 4(b) and 4(e)). Visibility is significantly improved when the linear cross-polarization arrangement is used (compare Fig. 4(c) and 4(f)) in accordance with the fact that polarization of the backscatter is mainly linear and in the same orientation of the incident light.

2.5. Tests in larger water tank

To validate the interest of using crossed linear polarization to eliminate backscatter effects, we extend our experiments to more realistic conditions. Tests were performed in a large water tank (Fig. 5(a)) of dimension [$3m \times 2m$] filled with natural water (5000*L*) to which we add skim-milk to mimic the turbidity conditions. Figure 5(b) shows the waterproof imaging system designed by FORSSEA Robotics Company [38]. This system contains a polarized light source and two cameras. The first is equipped with a polarizer fixed in the orthogonal state with respect to the state of the source. No polarizer is fixed on the second camera, this allows us to acquire two images of the scene at the same time (without and with polarization) in order to compare them. The linear crossed polarimetric imaging system was precisely calibrated in our laboratory (Fig. 5(c)).

Optics EXPRESS

Fig. 5. (a) Water tank [3m × 2m], (b) FORSSEA Robotics waterproof imaging system, (c) polarization calibration, (d) polarimetric imaging system and marker in the water tank.

On an optical bench, two polarizers were placed oppositely to each other and separated by a 30 *cm* distance. A linear polarization state is generated from the first polarizer illuminated by an He-Ne Laser source emitting at 632.8*nm*. The second polarizer (analyzer) can be rotated. Several markers were placed at the bottom of a large water tank at different distances, as shown in Fig. 5(d). Figure 6(a) is the unpolarized image of marker in clear water. Figures 6(b)–6(d) are the unpolarized images obtained when we added respectively 200*mL*, 400*mL* and 600*mL* of skim milk to 5000 *L* of clear water. The diffusion coefficients thus estimated are respectively ($\mu_{s1} = 0.016 cm^{-1}, \mu_{s2} = 0.032 cm^{-1}, \mu_{s3} = 0.048 cm^{-1}$). Figures 6(e)–6(h) show respectively the corresponding images taken at the same time with the crossed linear polarization.

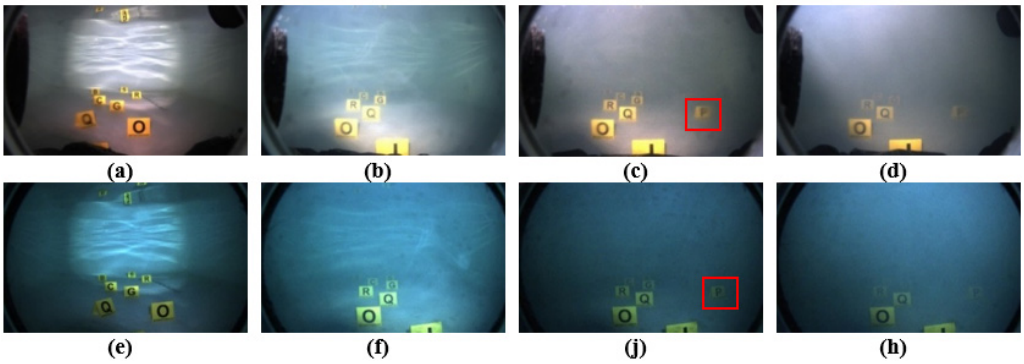

Fig. 6. Image of marker for different turbidity conditions (from left to right: (a) clear water, (b) turbidity μ_{s1} ,(c) turbidity μ_{s2} ,(d) turbidity μ_{s3} .Top row: unpolarized images, bottom row: the corresponding cross linear polarization images.

As can be seen from results, images taken using cross linear polarization have fewer reflections compared to raw images taken without polarized light. Consequently, letters on markers are clearly observed and easy to be distinguished in the cross linear polarization images. Figure 7 shows a comparison of the marker (framed in red) in Fig. 6(c) and Fig. 6(j).

Optics EXPRESS

Fig. 7. Image of marker (capital letter P) at turbidity μ_{s2}. (a) Without polarization. (b) With cross linear polarization.

Capital letter P is very blurred in the unpolarized image (Fig. 7(a)). A significant improvement in quality is observed when cross linear polarization is used (Fig. 7(b)). This clearly demonstrates the benefit of using polarization for improving the visibility and detection of markers. However, the visibility of the markers (especially the most distant ones) decreases when the concentration of milk in water is increased (Fig. 6(d)). In this case, polarization fails to totally remove the backscattering effect (Fig. 6(h)). Moreover, in real conditions, water depth and turbidity which mainly determine the light penetration will strongly limit the estimation of parameters of interest from the acquired image in test at sea. In the next sections, we introduce an innovative method that uses a combination of optical imaging polarimetry and dark channel prior (DCP) methods which enhance contrast in images of objects in turbid environments.

3. Optimized DCP-based method and experimental analysis

The dark channel prior (DCP) method has been heavily utilized in applications involving haze removal (dehazing) because it can significantly improve the quality of images of outdoor scenes. Basically, DCP relies on the fact that the intensity value of at least one color channel within a local window is close to zero. Based on the DCP, dehazing is accomplished through four steps: atmospheric light estimation, transmission map estimation, transmission map refinement, and image reconstruction [39].

3.1 Brief survey of DCP method

DCP is based on the following observation on outdoor haze-free images that in most of the non-sky patches at least one color (R, G, B) channel contains some pixels whose intensity are very low . To render observable this phenomenology, He and associates [7] introduced the concept of a dark channel for an arbitrary image J as:

$$J^{dark}(x) = \min_{y\in\Omega(x)}\left(\min_{c\in R,G,B} J^c(y)\right) \tag{26}$$

where J^c denotes a color channel of image and $\Omega(x)$ is a local window centered on pixel x. For our purpose, it is appropriate to use DCP in the model described by Eq. (3) to restore the radiance $J(x)$ of the scene. In order to get $J(x)$, A needs firstly to be estimated as follows: A^c is calculated on each channel by the average of the 0.1% I intensities corresponding to the brightest pixels in I^{dark} .Then, Eq. (3) is normalized to A^c according

$$\frac{I^c(x)}{A^c} = \frac{J^c(x)}{A^c}\cdot t(x) + 1 - t(x) \tag{27}$$

Now, introducing the dark channel operator (Eq. (26)) in both sides of Eq. (27), we find:

Optics EXPRESS

$$\min_{y\in\Omega(x)}\left(\min_{c\in R,G,B}\frac{I^c(y)}{A^c}\right)=\left\{\min_{y\in\Omega(x)}\left(\min_{c\in R,G,B}\frac{J^c(y)}{A^c}\right)\right\}t(x)+1-t(x) \tag{28}$$

Since $J(x)$ is the radiance of the scene without haze, the dark channel of $J(x)$ is close to zero. Hence, the multiplicative term in Eq. (28) can be ignored and the transmission $\tilde{t}(x)$ has the from:

$$\tilde{t}(x)=1-\min_{y\in\Omega(x)}\left(\min_{c\in R,G,B}\frac{I^c(y)}{A^c}\right) \tag{29}$$

Once A and the transmission map have been calculated, the image $J(x)$ is restored by making use of Eq. (3). Explicitly, one obtains:

$$J_c(x)=\frac{I_c(x)-A_c}{\max\left(\tilde{t}(x),\gamma\right)}+A_c \tag{30}$$

where γ is a parameter (set to 0.1) introduced to avoid out-of-range pixel values in the restored image. The DCP is effective in recovering bright colors and unveiling low contrast objects. However, it was found that the method presents two drawbacks which can lead to false detection of objects. Firstly, computing time increases with image size (typically 175 seconds for a 4K image). Secondly, the authors mention the appearance of block artifacts and halos due to the fact that the transmission is not always constant within a local window. To resolve this issue, they propose to refine the transmission map by a soft matting strategy [7]. Although satisfactory in many cases, a drawback of this additional treatment is an inherent increase of the amount of time it takes to run the algorithm which is unsuitable for real-time application. Additionally, this method is only effective for color images. In the next section, we propose and study an alternative algorithm which does not take into account colors to estimate the transmission map.

3.2 Optimized DCP-based method in context

Our method allows estimating the transmission map of the image by making use of a low-pass filter. In Eq. (3), backscattering light is modeled as:

$$I_B(x)=A\left(1-t(x)\right) \tag{31}$$

Thus, transmission $t(x)$ can be evaluated from $I_B(x)$ by:

$$\tilde{t}(x)=1-\frac{I_B(x)}{A} \tag{32}$$

It is often assumed that background light A can be estimated by the maximum pixel intensity in the image. Several methods have been proposed to estimate A in a more precise way. In [7], He and associates calculates A using the dark channel. Likewise, Kim and associates [40] propose to calculate A on the hazy area of the image. This region is obtained by subdividing the image in several regions and exploiting the fact that the variance of the pixel values is generally low in dense regions. However, such process is time consuming and unsuitable for our specific purpose. This paper assumes that A corresponds to the intensity of 0.1% times the brightest pixel of the image. Here, following the lead of Garcia and associates [16] we calculate the light illumination (which is a slowly-varying function in the image) from the input image I by a low-pass Gaussian filter G_σ as:

Optics EXPRESS

$$I_f(x) = G_\sigma \cdot I(x) \tag{33}$$

Where G_σ is a Gaussian function of standard deviation σ. We further allow $I_B(x)$ to be given by:

$$I_B(x) = I_f(x) - \sigma_f \tag{34}$$

Where σ_f is the standard deviation of the filtered image $I_f(x)$.Finally, once A and the transmission map $\tilde{t}(x)$ are known, we find that $J(x)$ can be obtained by inversing Eq. (3):

$$J(x) = \frac{I(x) - A}{\max(\tilde{t}(x), \gamma)} + A \tag{35}$$

Figure 8 summarizes the steps of our algorithm for grayscale images.

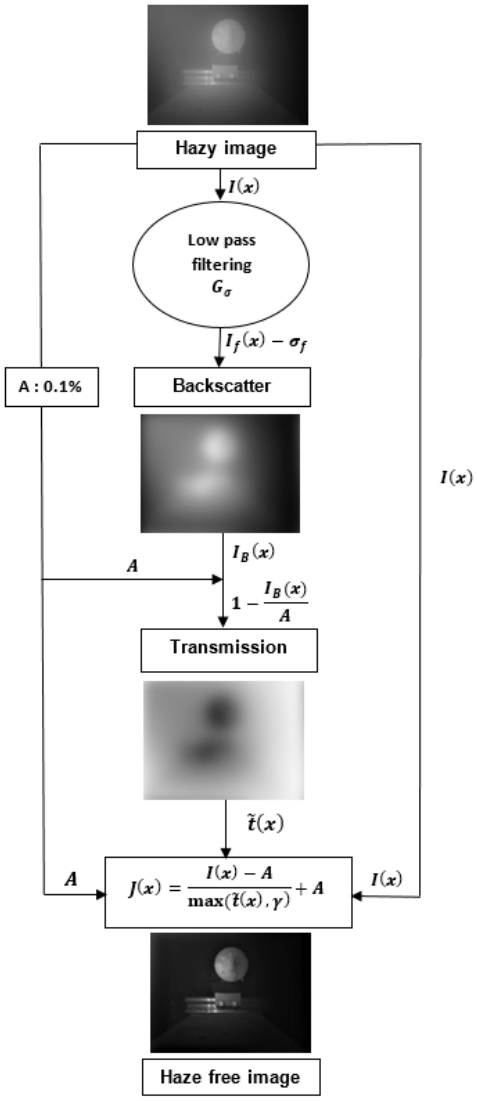

Fig. 8. Principle of our algorithm for grayscale images.

Optics EXPRESS

3.3 Validation tests for underwater grayscale images

To explore the performance of our algorithm tests are conducted on unpolarized images. Figure 9(a) shows the target image in clear water. Figures 9 (b) and 9(c) show the corresponding images for two turbidity cases, i.e. $\mu_s = 0.056cm^{-1}, \tau_0 = 1.96$ and $\mu_s = 0.084cm^{-1}, \tau_0 = 2.94$.

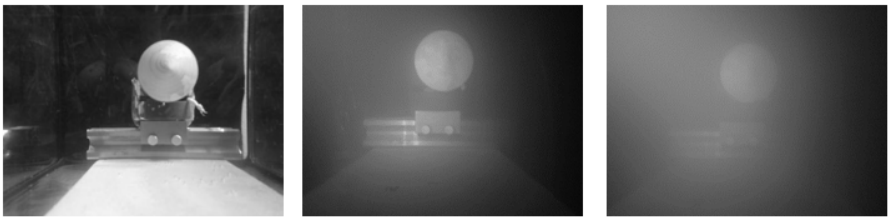

Fig. 9. Examples of image with different turbidity conditions: (a) target image in clear water, (b) target image in water tank with turbidity condition defined by $\mu_s = 0.056cm^{-1}, \tau_0 = 1.96$, when skim milk is added, and (c) as in (b) with turbidity $\mu_s = 0.084cm^{-1}, \tau_0 = 2.94$.

As is expected the intensity of the veil increases with water turbidity. In Fig. 10, we present a qualitative comparison for the improvement of quality of the images by making use of three methods: DCP, DCP with refinement of the transmission map by soft matting [7], and our approach.

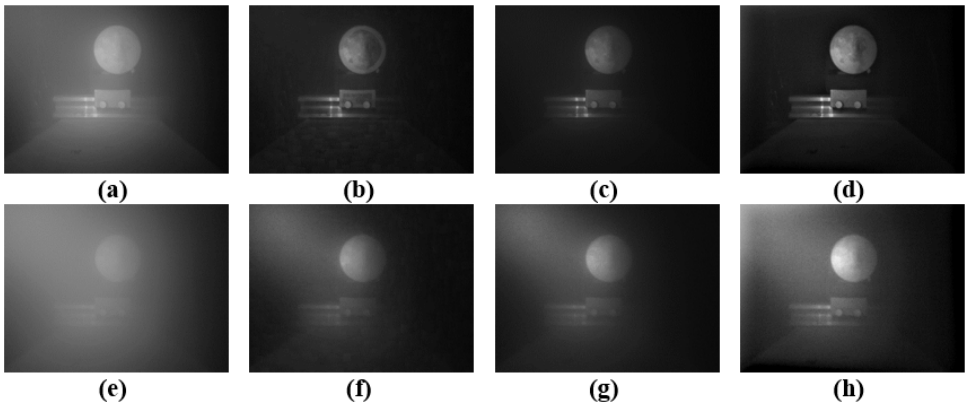

Fig. 10. The top row of each image block shows a comparison of the recovered images when the input image is Fig. 9 (a): (b) using DCP, (c) using DCP with refinement of transmission map by soft matting, and (d) using our approach. The bottom row shows a comparison of the recovered images when the input image is Fig. 9(c).

When viewing the results shown in Fig. 10, we observe that the DCP and our approach significantly reduced the veil and improved the target visibility. To quantitatively evaluate this improvement for the images shown in Fig. 10, the underwater image contrast measure (UIconM) is used:

$$\mathrm{UIconM} = \log\mathrm{AMEE}(\mathrm{I}) = \frac{1}{k_1 k_2} \otimes \sum_{l=1}^{k_1} \sum_{k=1}^{k_2} \frac{I_{\max,k,l} \Theta I_{\min,k,l}}{I_{\max,k,l} \oplus I_{\min,k,l}} \times \log\left(\frac{I_{\max,k,l} \Theta I_{\min,k,l}}{I_{\max,k,l} \oplus I_{\min,k,l}} \right) \tag{36}$$

Optics EXPRESS

where an image is divided into $k_1 k_2$ blocks, and $\otimes, \Theta, \otimes$ are the PLIP operations [41]. As can be seen in Table 1, a better contrast is obtained with our approach.

Table 1. UIconM values for images of Fig. 10.

	Figure 10(a)	Figure 10(b)	Figure 10(c)	Figure 10(d)
UIconM	**0.1431**	**0.2418**	**0.1637**	**0.2552**
	Figure 10(e)	Figure 10(f)	Figure 10(g)	Figure 10(h)
UIconM	**0.1044**	**0.2175**	**0.2021**	**0.2385**

Our overall estimate of the transmission map allows us to avoid the effects of windowing as is evidenced for the conventional DCP method (visible in Fig. 10(b)) which requires a map refinement by another algorithm such as soft matting (Fig. 10(c)). To illustrate further this point, Fig. 11 shows a comparison of the transmission maps obtained by the conventional DCP method (Fig. 11(b)) and our approach (Fig. 11(c)).

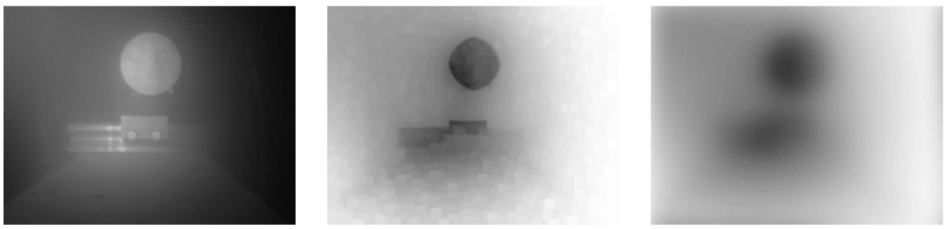

Fig. 11. (a) Input image. A comparison of transmission map between: (b) DCP and (c) our method.

In addition to gain in quality, an added benefit is that it is less computationally expensive than the DCP model, which allows for fast detection and recognition of objects. Our approach based on global filtering is much faster than the local calculation of dark channel. The runtime results in Table 2 show that our algorithm is much faster than the DCP algorithm. Hence, the proposed method significantly reduces runtime by a factor of about 50 for a 4K image compared to DCP.

Table 2. Comparison of algorithm runtime between conventional DCP method and our approach.

Image (i)	1	2	3	4	5
Image size	[644× 858]	[1287× 1716]	[1930× 2573]	[2573× 3431]	[3216× 4288]
Runtime (s) DCP	6.64	27.36	62.72	111.73	176.37
Runtime (s) our method	0.17	0.53	1.45	2.68	3.57

The low computational burden is important for optical-imaging applications where we desire real-time, high-quality color images. For this purpose, we now extend our approach to deal with color image processing. This method has been tested in experiment to determine sensitivity to turbidity. The results are shown to compare favorably with DCP data.

3.4 Validation tests for underwater color images

In this section, we present the details for how we execute the proposed algorithm shown in Fig. 12. Building on the algorithm described in Fig. 8 image data models $J_c(x)$ can be obtained for each individual color channel $c \in \{R, G, B\}$ in the form:

Optics EXPRESS

$$J_c(x) = \frac{I_c(x) - A_c}{\max(\tilde{t}_c(x), \gamma)} + A_c \tag{37}$$

These three images are then combined to give the improved color image output. Using this approach we can estimate for each channel *c* its own transmission map $\tilde{t}_c(x)$

$$\tilde{t}_c(x) = 1 - \frac{I_{Bc}(x)}{A_c} \tag{38}$$

where I_{Bc} and A_c are respectively the estimated backscattering component and the overall light for channel *c*. This approach is adapted to underwater images since the attenuation coefficients $\beta^R, \beta^G, \beta^B$ depend on wavelength. However, the three estimated transmission maps ($\tilde{t}_R, \tilde{t}_G, \tilde{t}_B$) introduce color distortion in the restored image. To avoid this problem, we consider for each pixel *x* the color for which the transmission is maximum, i.e. the less attenuated color. Thus, only a single transmission map is considered which can be represented by:

$$\tilde{t}(x) = \max\left[\tilde{t}_c(x)\right] = 1 - \min_x \left[\frac{I_{Bc}(x)}{A_c}\right] \tag{39}$$

The backscattering component I_{Bc} for channel *c* is defined as:

$$I_{Bc}(x) = I_{fc}(x) - \sigma_{fc} \tag{40}$$

where $I_{fc}(x)$ is obtained by a low-pass Gaussian filter of $I_c(x)$:

$$I_{fc}(x) = G_\sigma I(x) \tag{41}$$

and σ_{fc} is the standard deviation of the filtered image $I_{fc}(x)$:

Optics EXPRESS

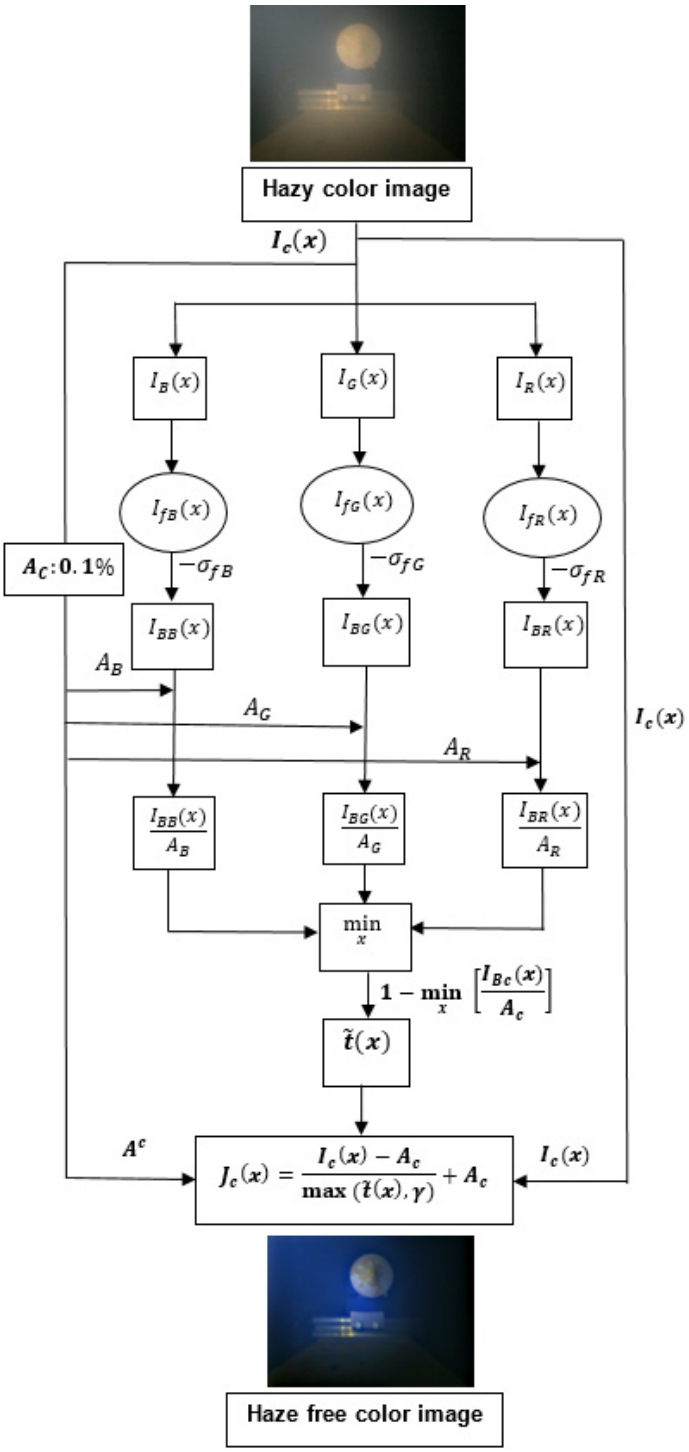

Fig. 12. Principle of our algorithm for color images.

Figure 13 shows the results of validation tests of our approach for color images. To compare our approach to the conventional DCP method and its extended version for color images, we consider data similar to those presented in Fig. 9.

Optics EXPRESS

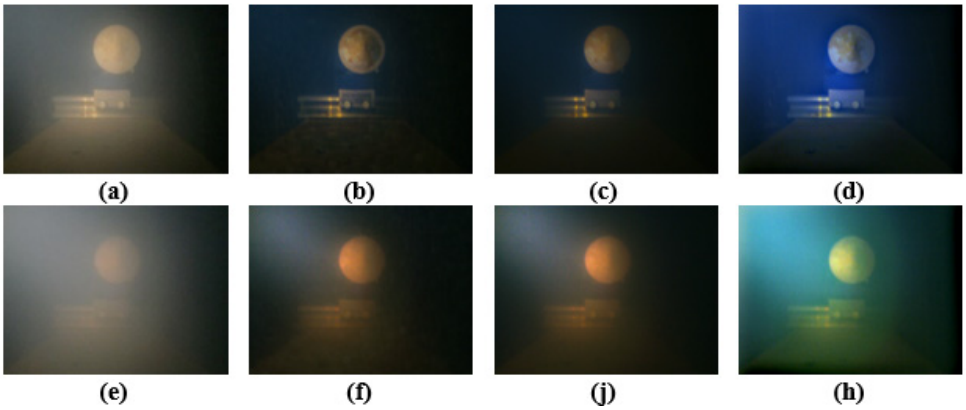

Fig. 13. The top row of each block of images shows a comparison of the recovered images when the input image is Fig. 9(a): (b) using DCP, (c) using DCP with refinement of transmission map by soft matting, and (d) using our approach. The bottom row shows a comparison of the recovered images when the input image is Fig. 9(c).

When viewing the example of Fig. 13, our method allows us to get a better contrast better than that obtained by the DCP and DCP with soft matting.

3.5 Validation tests for underwater grayscale polarized images

The examples in Fig. 10 and 13 show that our algorithm is able to significantly improve visibility of the images acquired in turbid optical media. In Fig. 14 we compare images of the target in turbid water acquired without polarization, with linear cross-polarization and linear cross-polarization using our processing method, respectively.

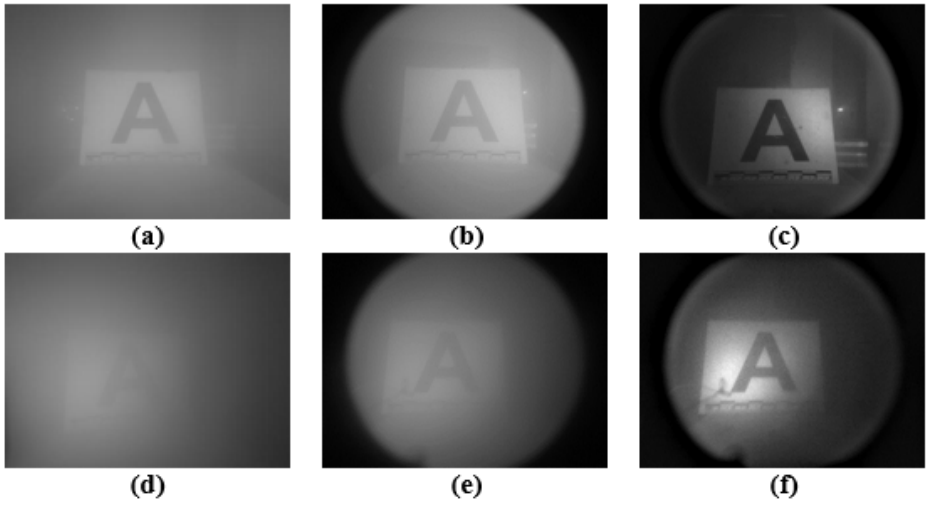

Fig. 14. The top row of each block of images corresponds to turbidity condition ($\mu_s = 0.056cm^{-1}, \tau_0 = 1.96$): (a) target image acquired without polarization, (b) target image acquired with linear cross-polarization, and (c) target image acquired with linear.

It can be seen from Fig. 14(b) and Fig. 14(e) that the veil is not completely filtered out and the contours of the target are not well defined by using linear cross-polarization. However, numerical improvement of these images (see Fig. 14(c) and Fig. 14(f)) by our method allows removing the remaining backscattering contribution and permits to significantly enhance the target contours.

Optics EXPRESS

4. Preliminary results from tests at sea

We show consider experimentally determined images obtained by tests at sea (bay area of Brest, France) in collaboration with FORSSEA Robotics which designed an autonomous docking underwater technology for AUVs based on our proposed method. This system was the subject of a patent (N/Ref: BG/EBU/DD-FR 1763336: DISPOSITIF D'AMELIORATION D'IMAGE SOUS-MARINE). This imaging system contains a polarized light source and two cameras. One is equipped with a polarizer oriented perpendicularly to the source polarization in order to acquire the linear cross-polarization image. No polarization filter is attached to the other camera. The system is connected to our boat in real time (Fig. 15).

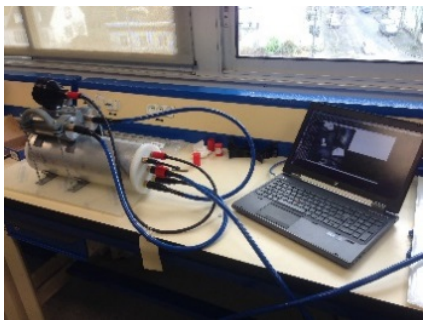

Fig. 15. Underwater imaging system.

The tests were performed in the port of Brest at night (http://www.google.fr/place/Brest). Preliminary results at 8 meters depth are shown in Fig. 16. Two targets are used to acquire test images. A swimmer adjusts the target-camera distance and stir the sand of the seabed to increase turbidity. 1379 [728× 1288] image size are acquired during this experiment. As can be seen from Fig. 16, a significant gain in quality is observed when the linear cross-polarization arrangement is used (Fig. 16(b)). The acquired images are much less affected by the veil of backscattering compared to those obtained without polarization (Fig. 16(a)). The additional processing of polarized images to fully remove the remaining backscattering contribution has the effect of significantly enhancing the contours of the target images (Fig. 16(c)).

Optics EXPRESS

Fig. 16. Results at 8 meters deep in the port of Brest at night. (a) Images acquired without polarization, (b) images acquired with linear perpendicular-polarization, and (c) images acquired with linear perpendicular-polarization and using our processing.

4. Concluding remarks and directions for further work

The novelty of this paper is to propose and study a relatively simple and computationally inexpensive yet effective algorithm for improving the quality of images in automating detection and recognition of objects under the surface of the water. The paper describes how to use a system of linear cross-polarization to filter out most of backscattering contribution during image acquisition and combining it to our numerical dehazing approach to these images. The latter assumes that backscattering is characterized by a low-frequency component which affects the image: this property is used as a prior (or knowledge) to estimate the transmission of the scene and restore the image from a simplified model of underwater image formation. The proposed method was tested in simulation and experiment over a range of conditions. It performs better than previously published dehazing algorithms in optical imaging applications. Based on its simplicity, consistency, and improvement in quality and algorithm runtime, this method is recommended for use in future real-time

Optics EXPRESS

automating image processing technique designed for detection and recognition of objects under the surface of the water. Future investigations of the effects of turbidity on the predictive method proposed here will explore approaches to circumvent current limitations in underwater imaging applications due to the blurring of the collected images. A complete description of the robustness of this approach for imaging in optically scattering media is under investigation. In this work, we focus on detecting relatively simple objects. Any future work will include more testing and validation with more complicated objects, e.g. underwater mines. Another continuing challenge in underwater optical imaging is the interpretation of the physical meaning of the Mueller matrix of an acquired image of a depolarizing object present in a turbid medium.

Funding

Institut Supérieur d'Electronique et du Numérique (ISEN-Brest), and also by Région Bretagne (ARED program).

Acknowledgments

The authors wish to thank Forssea Robotic Company that designed the polarimetric imaging system based on our proposed method, which was the subject of a patent (N/Ref: BG/EBU/DD-FR 1763336: DISPOSITIF D'AMELIORATION D'IMAGE SOUS-MARINE).

References

1. M. Legris, K. Lebart, F. Fohanno, and B. Zerr, "Les capteurs d'imagerie en robotique sous-marine : tendances actuelles et futures," Trait. du Signal **20**, 137–164 (2003).
2. A. Morel, "Optical properties of pure water and pure sea water," Opt. Asp. Oceanogr **1**(1), 1–24 (1974).
3. S. S. Sankpal and S. S. Deshpande, "A review on image enhancement and color correction techniques for underwater images," Advances in Computational Sciences and Technology **9**(1), 11–23 (2016).
4. R. Schettini and S. Corchs, "Underwater Image Processing : State of the art of restoration and image enhancement methods," EURASIP J. Adv. Signal Process. **2010**(1), 14 (2010).
5. J. S. Jaffe, "Computer modeling and the design of optimal underwater imaging systems," IEEE J. Oceanic Eng. **15**(2), 101–111 (1990).
6. Y. Y. Schechner and N. Karpel, "Recovery of underwater visibility and structure by polarization analysis," IEEE J. Oceanic Eng. **30**(3), 570–587 (2005).
7. K. He, J. Sun, and X. Tang, "Single image haze removal using dark channel prior," IEEE Trans. Pattern Anal. Mach. Intell. **33**(12), 2341–2353 (2011).
8. H. Lu, Y. Li, Y. Zhang, M. Chen, S. Serikawa, and H. Kim, "Underwater optical image processing: a comprehensive review," Mob. Netw. Appl. **22**(6), 1204–1211 (2017).
9. B. L. McGlamery, "A computer model for underwater camera systems," International Society for Optics and Photonics, In Ocean Optics VI. **208**, 221–231 (1980).
10. W. Hou, D. J. Gray, A. D. Weidemann, G. R. Fournier, and, J. L. Forand, "Automated underwater image restoration and retrieval of related optical properties," IGARSS (2007).
11. E. Trucco and A. T. Olmos-Antillon, "Self-tuning underwater image restoration," IEEE J. Oceanic Eng. **31**(2), 511–519 (2006).
12. B. Ouyang, F. R. Dalgleish, F. M. Caimi, A. K. Vuorenkoski, T. E. Giddings, and J. J. Shirron, "Image enhancement for underwater pulsed laser line scan imaging system," International Society for Optics and Photonics **8372**, 83720R (2012).
13. T. Treibitz and Y. Y. Schechner, "Active polarization descattering," IEEE Trans. Pattern Anal. Mach. Intell. **31**(3), 385–399 (2009).
14. J. V. C. I. R. A. Galdran, D. Pardo, A. Picón, and A. Alvarez-gila, "Automatic red-channel underwater image restoration," J. Vis. Commun. Image Represent. **26**, 132–145 (2015).
15. H. Lu, Y. Li, Y. Zhang, M. Chen, S. Serikawa, and H. Kim, "Underwater optical image Processing : a comprehensive review," Mob. Netw. Appl. **22**(6), 1204–1211 (2017).
16. R. Garcia, T. Nicosevici, and X. Cufi, "On the way to solve lighting problems in underwater Imaging," In Oceans'02 MTS/IEEE **2**, 1018–1024 (2002).
17. M. S. Hitam, " Mixture contrast limited adaptive histogram equalization for underwater image enhancement," Computer Applications Technology (ICCAT), 1–5 (2013).
18. A. Shahrizan, A. Ghani, N. Ashidi, and M. Isa, "Underwater image quality enhancement through integrated color model with Rayleigh distribution," Appl. Soft Comput. J **27**, 219–230 (2015).
19. C. Ancuti, C. O. Ancuti, T. Haber, and P. Bekaert, "Enhancing underwater images and videos by fusion," IEEE Conference on Computer Vision and Pattern Recognition. 81–88 (2012).

Optics EXPRESS

20. S. Bazeille, I. Quidu, L. Jaulin, and J.-P. Malkasse, "Automatic underwater image pre-processing," Cmm **06**(1), xx (2006).
21. I. Leonard, A. Alfalou, and C. Brosseau, "Sensitive test for sea mine identification based on polarization-aided image processing," Opt. Express **21**(24), 29283–29297 (2013).
22. M. Dubreuil, P. Delrot, I. Leonard, A. Alfalou, C. Brosseau, and A. Dogariu, "Exploring underwater target detection by imaging polarimetry and correlation techniques," Appl. Opt. **52**(5), 997–1005 (2013).
23. A. Kouzoubov, M. J. Brennan, and J. C. Thomas, "Treatment of polarization in laser remote sensing of ocean water," Appl. Opt. **37**(18), 3873–3885 (1998).
24. K. J. Voss and E. S. Fry, "Measurement of the Mueller matrix for ocean water," Appl. Opt. **23**(23), 4427–4439 (1984).
25. G. D. Lewis, D. L. Jordan, and P. J. Roberts, "Backscattering target detection in a turbid medium by polarization discrimination," Appl. Opt. **38**(18), 3937–3944 (1999).
26. L. Bartolini, L. De Dominicis, M. Ferri De Collibus, G. Fornetti, M. Francucci, M. Guarneri, E. Paglia, C. Poggi, and R. Ricci, " Polarimetry as tool to improve phase measurement in an amplitude modulated laser for submarine archaeological sites inspection," Proc. SPIE - Int. Soc. Opt. Eng **1** (7), 1–12 (2007).
27. G. D. Gilbert and J. C. Pernicka, "Improvement of underwater visibility by reduction of backscatter with a circular polarization technique," Appl. Opt. **6**(4), 741–746 (1967).
28. J. G. Walker, P. C. Chang, and K. I. Hopcraft, "Visibility depth improvement in active polarization imaging in scattering media," Appl. Opt. **39**(27), 4933–4941 (2000).
29. J. S. Tyo, D. L. Goldstein, D. B. Chenault, and J. A. Shaw, "Review of passive imaging polarimetry for remote sensing applications," Appl. Opt. **45**(22), 5453–5469 (2006).
30. J. D. van der Laan, D. A. Scrymgeour, S. A. Kemme, and E. L. Dereniak, "Detection range enhancement using circularly polarized light in scattering environments for infrared wavelengths," Appl. Opt. **54**(9), 2266–2274 (2015).
31. F. C. MacKintosh, J. X. Zhu, D. J. Pine, and D. A. Weitz, "Polarization memory of multiply scattered light," Phys. Rev. B Condens. Matter **40**(13), 9342–9345 (1989).
32. D. Bicout, C. Brosseau, A. S. Martinez, and J. M. Schmitt, "Depolarization of multiply scattered waves by spherical diffusers: Influence of the size parameter," Phys. Rev. E Stat. Phys. Plasmas Fluids Relat. Interdiscip. Topics **49**(2), 1767–1770 (1994).
33. G. W. Kattawar and M. J. Raković, "Virtues of mueller matrix imaging for underwater target detection," Appl. Opt. **38**(30), 6431–6438 (1999).
34. L. Mullen, B. Cochenour, W. Rabinovich, R. Mahon, and J. Muth, "Backscatter suppression for underwater modulating retroreflector links using polarization discrimination," Appl. Opt. **48**(2), 328–337 (2009).
35. S. Stocker, F. Foschum, P. Krauter, F. Bergmann, A. Hohmann, C. Scalfi Happ, and A. Kienle, "Broadband optical properties of milk," Appl. Spectrosc. **71**(5), 951–962 (2017).
36. Y. Piederrière, F. Boulvert, J. Cariou, B. Le Jeune, Y. Guern, and G. Le Brun, "Backscattered speckle size as a function of polarization: influence of particle-size and- concentration," Opt. Express **13**(13), 5030–5039 (2005).
37. http://www.sealife-cameras.com/fr/cam%C3%A9ras/dc1400-pro-vid%C3%A9o
38. http://www.forssea-robotics.fr/html/produit.html
39. S. Lee, S. Yun, J.-H. Nam, C. S. Won, and S.-W. Jung, "A review on dark channel prior based image dehazing algorithms," EURASIP J. Image Video Process. **2016**(1), 4 (2016).
40. J. H. Kim, W. D. Jang, J. Y. Sim, and C. S. Kim, "Optimized contrast enhancement for real-time image and video dehazing," J. Vis. Commun. Image Represent. **24**(3), 410–425 (2013).
41. K. Panetta, C. Gao, and S. Agaian, "Human-visual-system-inspired underwater image quality measures," IEEE J. Oceanic Eng. **41**(3), 541–551 (2016).